Renewable Energy 225 (2024) 120332

Contents lists available at ScienceDirect

Renewable Energy

journal homepage: www.elsevier.com/locate/renene

High-resolution spectral atmospheric attenuation measurement for solar power plants

Carlos Heras [a,*], Iñigo Salinas [a], Salvador Andres [b], Marina Sevilla [b], Asier Villafranca [b], David Martinez [a], Marcelino Sanchez [c]

[a] Aragon Institute of Engineering Research (I3A), Universidad de Zaragoza, C/Mariano Esquillor, 50018, Zaragoza, Spain
[b] Zepren Solutions S.L. Pol. Ind. Royales Bajos, S/n, Puebla de Alfindén, 50171, Zaragoza, Spain
[c] National Renewable Energy Centre (CENER), C/ Ciudad de La Innovación 7, 31621, Sarriguren, Spain

ARTICLE INFO

Keywords:
Atmospheric attenuation measurement
Central receiver CSP
VIS-IR optical spectrum measurement
Global solar energy measurement
Atmospheric attenuation modeling
Solar tower plants

ABSTRACT

One of the main challenges in solar tower renewable technologies is measurement of solar radiation attenuation at the plants at surface level. This paper describes an improved version of the optical spectrum analysis method for measuring solar radiation attenuation in real time at solar tower plants, as presented in a previous work. The new hardware design and calibration process are explained in detail. This new system has a resolution of 0.25 nm in the VIS range and a precision of 0.5% in real time, improving over the state of the art for the measurement of spectral atmospheric attenuation. These specifications allow the assessment of the contribution of different attenuation factors at surface level, such as absorbance peaks (Na, H, H_2O) or scattering and the search for correlation with different weather conditions. They also enable experimental validation of atmospheric extinction simulation methods and their parameters. This work also includes the results of a 6 month-long campaign of solar weighted atmospheric extinction measurements at Atlantica's operating central receiver solar plant PS10 at Sanlúcar la Mayor (Seville, Spain). Fluctuations in the daily averaged transmittance greater than 10% are observed, which shows the importance of monitoring this parameter during the operation of solar plants.

1. Introduction

Solar radiation in solar tower plants is attenuated between the heliostat field and the receiver due to atmospheric extinction [1]. Atmospheric extinction is caused mainly by aerosol particles and water vapor, which scatter and absorb solar radiation [2]. This process is variable with site and time. Several theoretical approaches have been presented in the literature to determine site-dependent extinction time series based on different on-site standard atmospheric conditions and models [3,4]. Experimental approaches to resolve atmospheric extinction from ground measurements have also been published. Some of them use scatterometers that can be easily mounted and determine the atmospheric scattering mainly by aerosol particles in a small air volume. Radiative transfer calculations and absorption and broadband corrections translate measured values of the scatterometers into the broadband transmittance for the length of the solar plant, which is of interest for resource assessment for CSP projects [3,5–8].

Other experiments measure radiation emitted by a controlled light source along a path on different locations of the plant and evaluate the atmospheric extinction by comparison of this measured radiation at different sites. These setups rely on direct measurements and should result in more realistic atmospheric extinction values. Many of them use pyrheliometers and transmissometers to record the DNI [9] and derive the extinction coefficient. An approach based on digital cameras by simultaneously taking pictures of a white target from different distances was also reported to approximate the extinction ratio [10,11]. In 2022 we presented an atmospheric extinction measurement concept based on optical spectrum analysis [12]. It includes visible (VIS) and near infrared (NIR) wavelength ranges for the atmospheric extinction evaluation to prevent inaccuracies due to wavelength dependencies of the contributions to the measurement [13,14]. Atmospheric attenuation spectral curves of 5 nm resolution in visible and 10 nm resolution in infrared ranges were reported and atmospheric extinction values within 1% accuracy were obtained.

As it is well-known, there are important difficulties for the validation of these experiments. First, the measured extinction values cannot be

* Corresponding author.
E-mail addresses: cdheras@unizar.es (C. Heras), isalinas@unizar.es (I. Salinas), sandres@zepren.com (S. Andres), msevilla@zepren.com (M. Sevilla), asier@zepren.com (A. Villafranca), josedavid.martinez@unizar.es (D. Martinez), msanchez@cener.com (M. Sanchez).

https://doi.org/10.1016/j.renene.2024.120332
Received 25 September 2023; Received in revised form 16 February 2024; Accepted 13 March 2024
Available online 18 March 2024
0960-1481/© 2024 The Authors. Published by Elsevier Ltd. This is an open access article under the CC BY license (http://creativecommons.org/licenses/by/4.0/).

compared to a reference standard to assess their accuracy or calibrate the system. Also, the presence of moving clouds during the measuring time interval can result in incorrect atmospheric extinction values [15]. The former problem cannot be easily solved, but on one hand we have enhanced the resolution of the equipment to better resolve particular behaviors of attenuation curves to show the high consistency of the method and, on the other hand, we have introduced a new calibration process to provide a more reliable reference for the measurements. The second one can be mitigated using an estimation of the confidence intervals of each measurement.

In this work we describe the improved implementation of an optical spectrum analysis method for the attenuation extinction measurement in solar plants [12,16]. It includes a hardware redesign and new strategies in the measurement and the calibration processes. It also incorporates analysis algorithms to evaluate the reliability of the reported values. The new system achieves a spectral resolution of 0.25 nm and a precision of 0.5% in the VIS region.

This kind of detail and precision in the measurement of spectral atmospheric attenuation in solar plants provides the capability to better assess the different sources of attenuation, such as peaks of absorbance or scattering. For the first time, the atmospheric absorption due to the presence of molecules such as H_2O or O_2 is measured with good correlation to weather conditions, illustrating the possibilities of this system.

This system also opens the way to experimentally validate values of the characteristic parameters of the different aerosol models used by the atmospheric extinction simulations proposed in the literature, such as Angstrom's wavelength exponent and molecular absorption cross-sections that are used in SPCTRAL2 and MODTRAN models as discussed in Refs. [17,18] respectively. Achievable precision of 0.5% in the weighted solar attenuation value and the confidence algorithms for each value in real time make the system a useful tool for the operation of CSP plants.

A 6-month campaign of measurements in a commercial solar thermal power plant, Atlantica's central receiver system PS10 at Sanlúcar la Mayor (Seville, Spain), is presented as a sample of the possibilities of the improved system. Fluctuations in the daily averaged transmittance greater than 10% are observed, which shows the importance of monitoring this parameter for the operation of the solar plants. Also, relevant spectral features in some singular weather conditions during the long-term campaign are detailed as examples of the capacities. For reasons of confidentiality, reported dates are not exact and all absolute attenuation values have the same arbitrary offset inside 2%.

2. System description

2.1. Measurement setup

The atmospheric extinction measurement setup uses two diffuse screens, black and white, reflecting the radiation from the sun, and two optical devices to measure the spectrum of that reflected radiation. The basics of this system were previously described in Ref. [12]. The optical devices include an optical module and a detection module with VIS and NIR spectrometers. One of the devices (*Reference*) is located at a short distance from the screens to obtain a reference measurement. It eliminates any dependence with the sun and the air mass on the way from the sun to the ground level. The other one (*Tower*) is located at a larger distance (ideally around 1 km). The ratio between the spectra measured by the two devices provides the attenuation spectrum of the atmosphere in the distance between the two locations. The light background level for both devices is accounted for in a measurement using the black screen.

The system has been installed in the PS10 central receiver CSP plant, and its basic diagram is shown in Fig. 1. Both diffuser screens are located at the end of the plant and south oriented, just behind the last line of heliostats. The *Reference* device is located at a 50 m distance from it, whereas the *Tower* device is located at middle height level at the Atlantica solar tower, both north oriented and protected from weather conditions. The devices have 4G data connection for real time control and data report. The main control unit is integrated in the device placed at the tower, and can also be connected to a remote PC access for control or measurement analysis.

2.2. Equipment

The wavelength resolution was formerly limited to 5 nm in the VIS range due to the available intensity level of the radiation incoming from the screens on the *Tower* device. Although that wavelength resolution was enough to offer 1% precision on the weighted solar attenuation value, it was insufficient for the analysis of the subtle features of the transmittance spectra such as absorbance peaks or the scattering dependence versus wavelength. In this work, we have redesigned the optics of the *Tower* device to increase the intensity reaching the spectrometers. This new optical scheme is detailed in Fig. 2 and the layout of the main components of the optical and mechanical design for the *Tower* device is shown in Fig. 3a.

The optical setup consists of a Newton reflecting telescope with a primary mirror with a diameter of 254 mm and $f = 1200$ mm focal length and a secondary concave mirror with a diameter of 25 mm to gather a large amount of light coming from the object with a minimum occlusion. A diaphragm is placed at the image plane of this telescope for

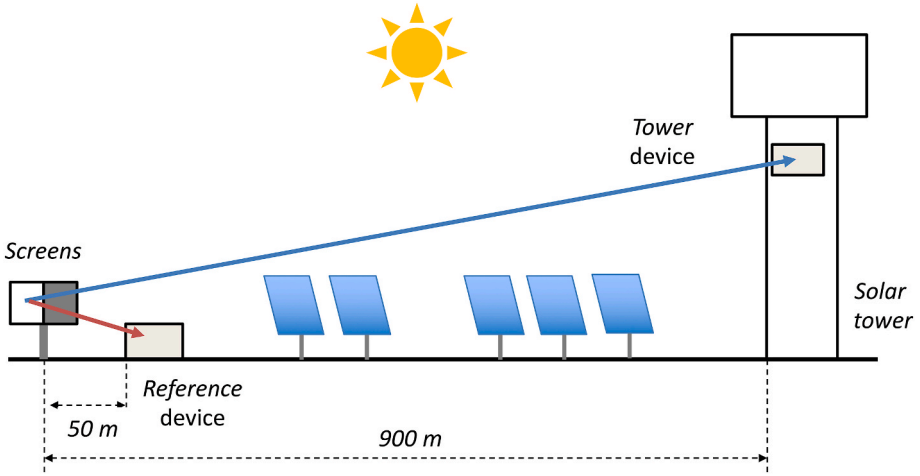

Fig. 1. Basic diagram of the system installed in the operating solar plant.

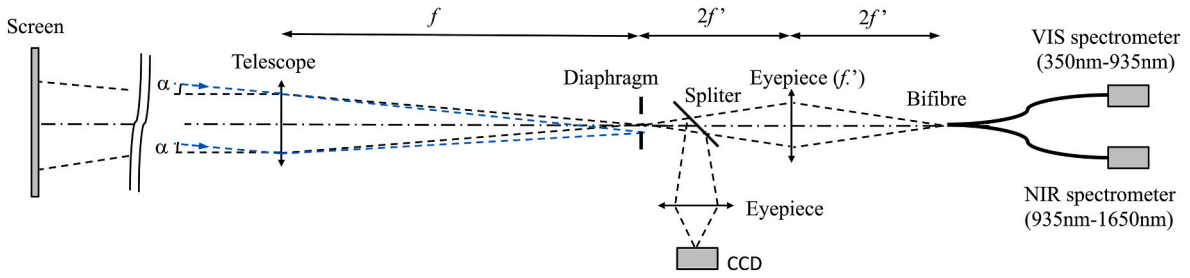

Fig. 2. Basic optical scheme of the *Tower* and *Reference* devices.

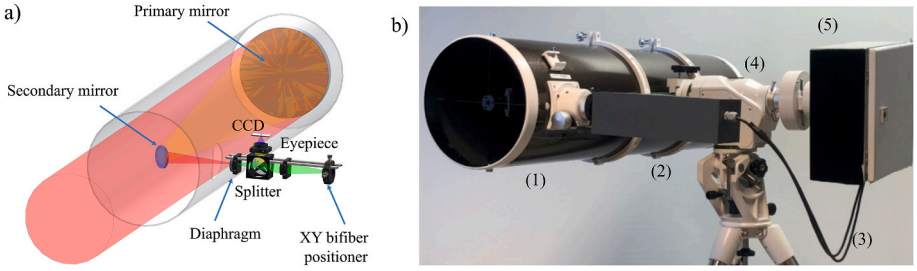

Fig. 3. *Tower* device. a) Layout of the main components. b) Photo of the device and the motorized mount: (1) Newton telescope, (2) eye piece module with diaphragm, CCD camera and bifiber positioner, (3) bifiber, (4) motor mount, (5) detection module with VIS and IR spectrometers.

an easy alignment of the system during the installation process. After it there is a $f' = 50$ mm focal eyepiece working with 1:1 magnification (image distance and object distance of 100 mm). It forms the image of the screen on a 1 mm diameter two-fiber bundle. Compared to the previous design, the intensity reaching the spectrometers is increased approximately by a factor of 8, making possible the use of the full resolution of the VIS spectrometer device (approximately 0.25 nm). A 10/90 splitter is used to take a real time image of the screens on a CCD camera for alignment purposes. An image captured by the camera after the diaphragm is shown in Fig. 4a. The green square is generated by a digital image processing algorithm that locates the center of the screen. The blue lines mark the center of the fiber bundle on the object image. This position is optically determined during the installation process by pointing the telescope to the center of the white screen, closing the diaphragm down to 1 mm (the diameter of the fiber, so that $\alpha \cong 0.5$ mrad) and maximizing the intensity in the spectrometers using the XY translation mount of the bifiber positioner to align the bifiber position in the optical axe. The red circle shows the area captured by the telescope according to the aperture angle of the optical system.

The *Tower* device is placed on an azimuth-elevation motorized mount with <0.001 mrad resolution in both the azimuth and elevation axes (Fig. 3b). Using the digital image from the camera, the system automatically points the *Tower* device to either the center of the white or the black screen during the measurement process. The motorized mount provides a very precise alignment of the optical system with the screens, which is obviously required for high precision measurements. In Fig. 4b we show an azimuth-elevation scanning test on the white screen. The telescope is centered on different points of the white screen and the signal intensity at 550 nm for each of these points is recorded. The figure represents the measured signal (relative to the maximum) for the complete screen area, equivalent to a range of 3000 × 3000 motor steps, in 300 motor step intervals. This scanning test was carried out 6 moths after installation to study the effect of the exposure to the elements on the uniformity of the white screen. In case of a deviation over 1% in the reflectance uniformity of the central area, an alert message recommending a screen repaint is sent.

At the *Reference* device, the intensity of the incoming radiation is not an important limitation. Nevertheless, its optics has been also redesigned and simplified. The new optical scheme is the same that was shown in Fig. 1 for the *Tower* device, whereas the layout of the main components is detailed in Fig. 5a). A refractive telescope with a lens of diameter 50 mm and focal length 300 mm captures the light reflected at the screens and an eyepiece identical to the one in the other device takes it to a two-fiber bundle. The optical module is also mounted on an

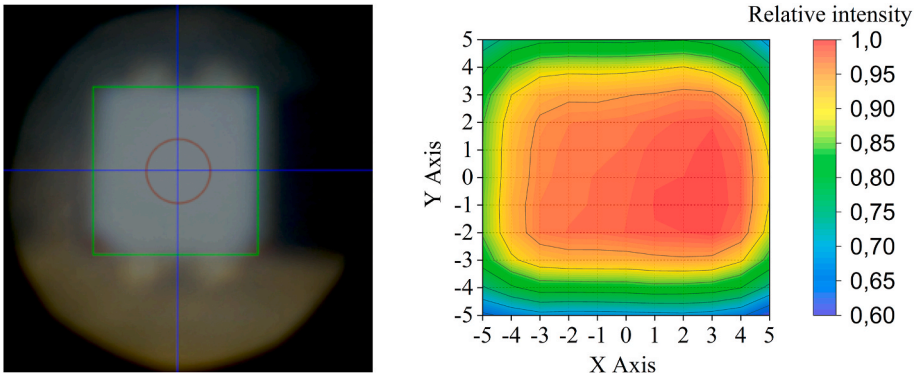

Fig. 4. a) Image of the white and black screens captured by the camera on the *Tower* device. b) Measured uniformity in the azimuth-elevation scanning test of the white source from the *Tower* device.

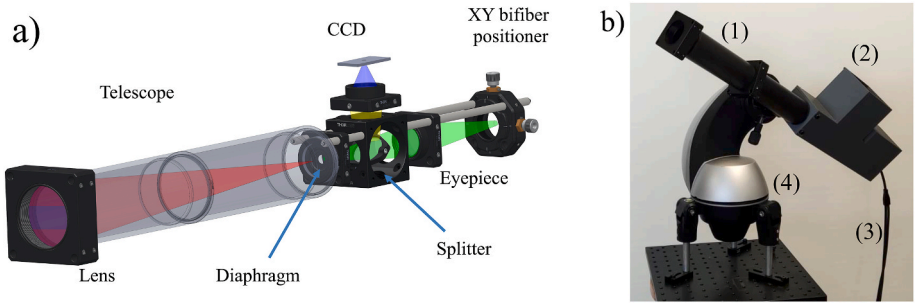

Fig. 5. *Reference* device. a) Layout of the main components of the *Reference* device. b) *Reference* device and motorized mount: (1) refractive telescope, (2) eye piece module, diaphragm, CCD camera and bifiber positioner, (3) bifiber, (4) mount.

azimuth-elevation motorized mount with <0,003 mrad resolution (Fig. 5b). The system automatically and sequentially points the *Reference* device to the center of the white and the black screen during the measurement process.

2.3. Accuracy and resolution of the spectral measurements

As indicated in our previous work, the large dependence with wavelength of the sun radiation intensity impacted the spectral measurements accuracy and resolution. In this work we have enhanced them, in addition to the redesign of the optics, by using a measurement process with different integration times for different VIS wavelength ranges, as detailed in Table 1. The new measurement process is as follows: first, we determine the integration time for the VIS2 range in order to put the maximum measured intensity between 35.000 a. u. and 40.000 a. u. Thus, the intensity is inside the most linear response zone of the spectrometers (10.000 a. u. to 40.000 a. u.). Second, this integration time, multiplied by a constant factor, is used to measure the VIS1 and the VIS3 ranges. At each of the three VIS wavelength ranges, measurements are averaged during 1 s. Thus, we maintain the level of the spectral curves in the most linear response zone even in the wavelength ranges with low sun radiation power. Some of the attenuation peaks of interest are located at this ranges. For the IR spectrometers, we maintain a constant integration time of 5 s over their full wavelength range. The overall measurement process lasts less than 20 s including alignment movements.

Fig. 6 shows a repeatability test with the estimation of the uncertainty at each wavelength. It includes the standard deviation obtained for 10 measurements over 5 min from the *Tower* device pointing at the white screen in a clear day. Table 2 reports the calculated percent relative standard deviation in the different wavelength ranges. Note that the lower accuracies belong to the wavelength ranges with lower sun radiation intensity, and thus with minimal impact on the solar weighted extinction coefficient.

2.4. Calibration process

A new calibration process has been introduced to improve the accuracy of the absolute attenuation extinction value. The previous calibration process required moving the *Reference* device close to the *Tower* device, which is a complicated task and can introduce errors due to potential misalignments of the optics. To avoid this step, we have developed a portable calibration device, which can be easily moved between the locations of the other two devices. The optical design is the same of the *Reference* device (Fig. 5a) and the spectrometers are also stabilized in temperature to 27 °C. In Fig. 7 we show the two steps of the calibration process. First, in the tower location (Fig. 7a), a diffuse white screen is placed in front of the *Tower* and calibration devices, and both measure simultaneously the sun radiation reflected by the screen, $S_{tow}(\lambda)$ and $S^{tow}_{cal}(\lambda)$. Then, at the *Reference* location (Fig. 7b), the process is repeated using the *Reference* and calibration devices to obtain the spectra $S_{ref}(\lambda)$ and $S^{ref}_{cal}(\lambda)$. Thus, the calibration device measurements allow us to establish the ratio $K(\lambda)$ between the responses of the *Reference* and *Tower* devices at each wavelength from Eq. (1):

$$K(\lambda) = \frac{S_{ref}(\lambda)/S^{ref}_{cal}(\lambda)}{S_{tow}(\lambda)/S^{tow}_{cal}(\lambda)} \quad (1)$$

2.5. Weighted atmospheric transmittance calculation

Once calibrated, the measurement process is simple. The *Tower* and *Reference* devices, each at their corresponding locations, are pointed to the white screen to obtain two different spectral measurements, $S^{w}_{tow}(\lambda)$ and $S^{w}_{ref}(\lambda)$. After that, both devices are pointed to the black screen to take another two measurements, $S^{b}_{tow}(\lambda)$ and $S^{b}_{ref}(\lambda)$, in order to determine the background light at that moment, mainly due to the diffuse light existing in the plant. Thus, the atmospheric transmittance at each wavelength $T(\lambda)$ is given by Eq. (2).:

$$T(\lambda) = \frac{S^{w}_{tow}(\lambda) - S^{b}_{tow}(\lambda)}{S^{w}_{ref}(\lambda) - S^{b}_{ref}} \bullet K(\lambda) \quad (2)$$

The solar weighted atmospheric transmittance T is given by Eq. (3)

$$T = \int_{\lambda_0}^{\lambda_f} T(\lambda) \bullet S_{sun}(\lambda) \quad (3)$$

Where $S_{sun}(\lambda)$ is the normalized reference solar spectral irradiance (in our case, using ASTM standard G173-03) and λ_0 and λ_f are the limits of the considered wavelength range.

3. Results

The new devices have been installed in Atlantica's central receiver system PS10 at Sanlúcar la Mayor (Seville, Spain), in the same locations of the 2021 setup, for a long-term measurement campaign in order to evaluate the performance of the system in an operating commercial solar plant. Some details of the installation (*Tower* device and white and black screens) are shown in Fig. 8.

For a better understanding of the results, we first highlight the spectral features of the measured atmospheric transmittance $T(\lambda)$. Then, we present the results of the six-month measurement campaign sum-

Table 1
Spectrometer measurement parameters for the different wavelength ranges.

wavelength range	wavelength range	integration time factor	measurement time
VIS1	350 nm–450nm	x2	1s
VIS2	450 nm–600nm & 600 nm–750nm	x1	1s
VIS3	750 nm–900nm	x3	1s
IR	900 nm–1650nm	–	5s

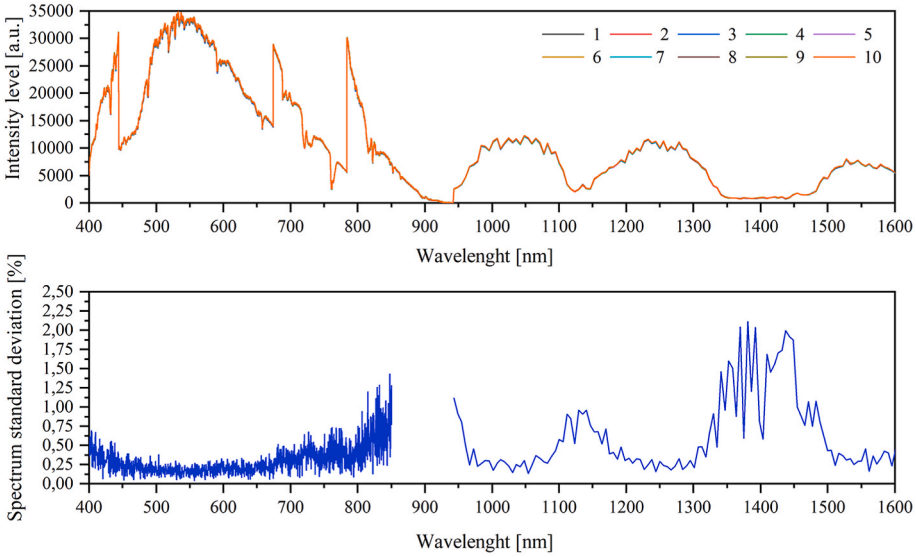

Fig. 6. Ten consecutive spectra and their percent relative standard deviation.

Table 2
Percent relative standard deviation measured values for the different wavelength ranges.

< 0,5 %	<1 %	>1%	≫1%
450 nm–725nm 960 nm–1100nm 1160 nm–1300nm 1500 nm–1650nm	400 nm–450nm 725 nm–850nm 1100 nm–1160nm 1300 nm–1350nm 1460 nm–1500nm	<400 nm 1350 nm–1460nm	850 nm–950nm

marized in the evolution of the solar weighted atmospheric transmittance. We also compare the spectral features of measurements belonging to different hours and days and, finally, we show in detail days with specific humidity and haze conditions, which introduce changes in the transmittance spectrum that can clearly be detected with our system.

3.1. Spectral features of the measured atmospheric transmittance

An example of the typical atmospheric transmittance $T(\lambda)$ measured in sunny conditions is shown in Fig. 9 and compared with a typical ground level atmospheric transmittance spectrum calculated using MODTRAN. The grey line is the spectral measurement of the reflection on the white screen, similar to that shown in Fig. 6. The red line corresponds to the transmittance data calculated using wavelength steps of 0.25 nm and 5 nm for VIS and IR respectively. A moving average over 4 data points has been used to avoid artifacts due to small differences between the exact wavelengths used by each device.

Note that no values are reported in the 900–950 nm and 1360–1450

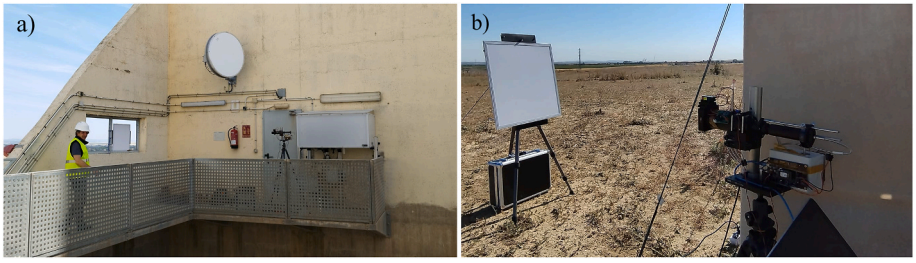

Fig. 7. Calibration set-up photos.

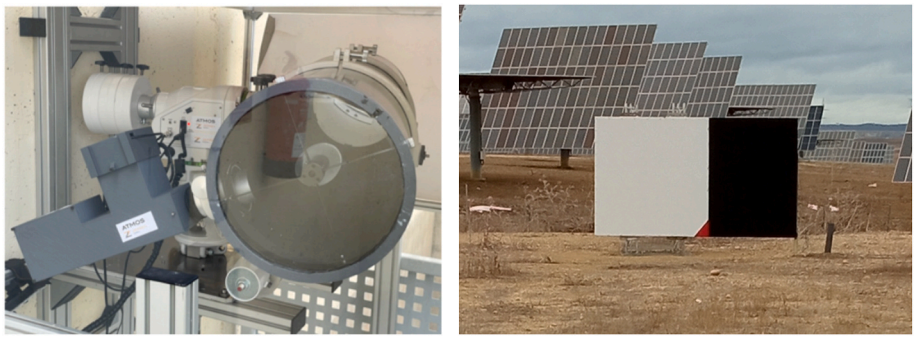

Fig. 8. Installation of the 2023 system.

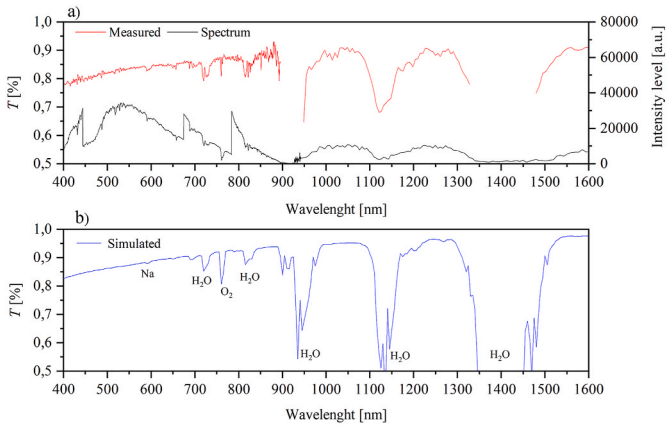

Fig. 9. a) Measurement of the solar spectrum and the spectral atmospheric transmittance (T = 30 °C, RH = 40%, WS = 10 km/h). b) Atmospheric transmittance simulated using MODTRAN.

nm ranges because of the lack of accuracy due to the low intensity of sun and the low response of the spectrometers in these wavelengths.

The measured spectral pattern is very similar to the simulated one. In the VIS range, the optical transmittance follows a relatively smooth increase with wavelength that can be approximated to a power-law wavelength dependence due to the scattering of small air particles [19]. It also shows the most relevant absorbance peaks produced by the presence of different molecules in the air at their corresponding wavelengths, as depicted in the figure.

It is well known that these features of the spectral transmittance curves evolve with weather conditions due to the changes in size of the scattering particles and the presence of absorptive molecules [19]. Several simulations, computed with MERRA, MODTRAN or similar software, have been reported in the literature for different weather and site conditions [20] showing tendencies that correlate to our experimental observations along the measurement campaign.

3.2. Measurement campaign

Fig. 10 is a summary of the results obtained in the six-month measurement campaign. In this figure, we show the day-averaged solar weighted atmospheric transmittance *T*. Each measured value is also given with its standard deviation along the same day. A large standard deviation indicates notable differences in the transmittance *T* during

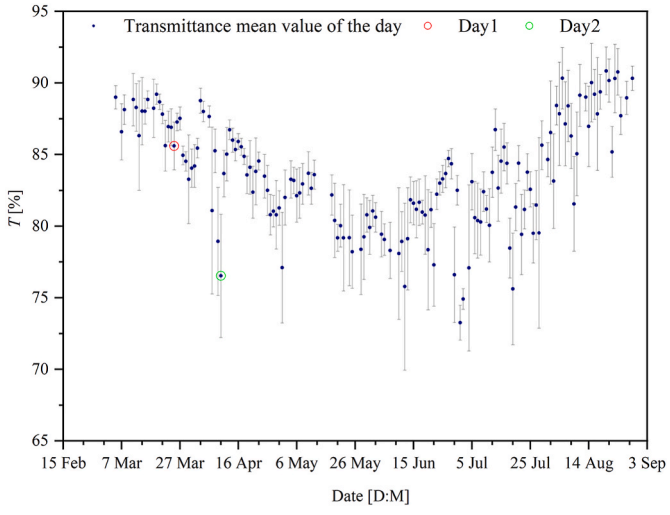

Fig. 10. Daily averaged measured solar weighted atmospheric transmittance in the six-month campaign and its standard deviation along the same day.

that day, whereas a small standard deviation belongs to a day with stable weather conditions. Note that these averages are calculated considering only values accepted by a validation algorithm, and days without data are cloudy days with no values reported as valid. Also, transmittances are offset by a constant value to protect the confidentiality of the information on the solar plant.

Between days, variations of the daily averaged transmittance greater than 10% are observed, which shows the importance of monitoring this parameter for the operation of the solar plants. A significantly smaller transmission can be observed in the early summer months (May, June), probably because of higher concentration of Saharan dust in the air. Nevertheless, this analysis is beyond the scope of this work, and these conjectures should be correlated with dust and air particles analysis in field.

As it has pointed before, our system includes real-time data evaluation to detect and discard insufficiently precise measurements, as avoiding the report of incorrect values is key for the operation of the plant. Since the measurement is averaged over 1 s, the standard deviation of the detected power at 550 nm during the measurement process can be calculated to provide the confidence interval for each measurement. This value, as well as the recent transmittance values and the spectral shape of measured intensity curves, is then considered to validate the measurement. Thus, we can detect rapid changes of intensity that can occur due to clouds shading the screens or other intermittent atmospheric phenomena during a measurement. As an example of this validation algorithm, Fig. 11 shows the measured transmittance values, in 5-min interval, during a sunny day a) and a sunny day with sparse clouds b). Each measured value is given with its confidence interval, and those that are reported as correct by the validation algorithm are marked with green circles. This information is available in real time.

Spectral features at different hour and days can also be compared. Fig. 12 shows some measured transmittance spectra in the VIS and IR ranges as examples of the ability to discriminate between different conditions. The data correspond to different hours over three days, and the corresponding local weather conditions are reported in Table 3. The VIS curves clearly have different slopes, which is in accordance with the changes predicted in the literature for the exponent of the function describing the dependence of atmospheric aerosols scattering with the size of the air particles existing at ground level in the solar plant.

Fig. 13 shows details of some relevant absorption peaks in the VIS range for different moments over two days. These graphs were obtained using a normalization to better compare the absorption peaks by eliminating the influence of other factors. In the case of the Na peak, no significant variations are observed with time, whereas O_2 and H_2O peaks show different magnitudes between measurements that can be correlated with the different weather conditions.

Each day can also be analyzed individually in detail. Relevant examples are shown in Figs. 14 and 15 which correspond to the days marked in Fig. 10 with a red (day 1) and green circle (day 2).

Day 1 is a day with a humid morning, and its graphs show that variations in the air humidity throughout the day (also shown in the figure) impact the evolution of both the atmospheric transmittance *T* and the H_2O absorption peaks. A variation in transmittance near 10% is measured between the hours with high and low humidity. The evolution of the water absorption peak size is also in correlation with the weather report.

Day 2 (Fig. 15) is a hazy day due to the presence of suspended desert dust particles in the air. The wind velocity report for the day is also shown in Fig. 15a. At the hours with haze, the transmittance significantly decreases compared to a clear day, while at the evening hours (due probably to the rising wind) it increases near a 15% to return to usual values. Haze has a singular effect on the shape of the spectral transmittance (Fig. 14b). The slope of the transmittance curve decreases in the short wavelength range, compared to non-hazy days like those on of Fig. 10. This behavior is probably related to particle size [19,21–23]. In the case of large particles present in the air, the Angström exponent is

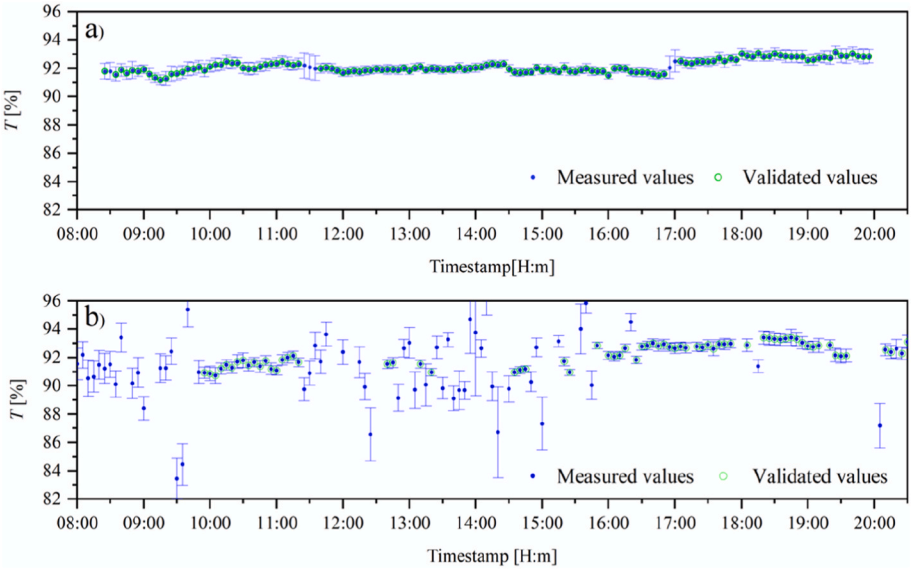

Fig. 11. Measured transmittance values and validation algorithm during a) a sunny day, b) a day with sparse clouds.

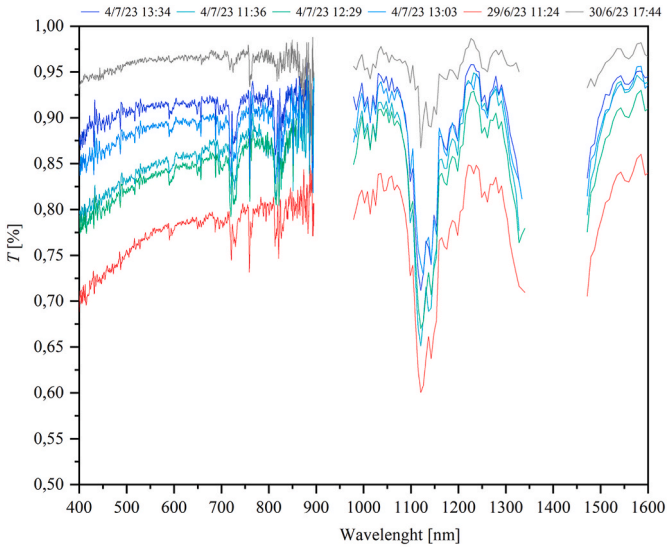

Fig. 12. Measured atmospheric transmittance $T(\lambda)$ at three different days and different hours.

Table 3
Local weather conditions for different hour/days.

Hour/day	Temperature (°C)	Relative Humidity (%)	Wind Speed (km/h)
29/6/23 11:30	28	70	15
30/6/23 17:44	28	22	22
4/7/23 11:36	28	57	12
4/7/23 12:29	30	55	15
4/7/23 13:03	32	45	17
4/7/23 13:34	35	40	20
6/7/23 14:54	36	28	16
6/7/23 16:52	34	20	21

close to 1 and the scattering component of the extinction coefficient becomes quite independent of wavelength.

These results validate the potential use of the system as experimental aid for atmospheric extinction simulations and studies, and provide a high level of confidence in its value as a spectral atmospheric attenuation measurement system for commercial solar plants. The precision of our system clearly allows for a study of the evolution of scattering and absorption peaks and the search for correlation with different weather conditions. This capability can be used, along with other measurement devices, to fine tune simulation parameters.

4. Conclusions

An improved implementation of the optical spectrum analysis method for the attenuation extinction measurement in solar plants has been presented. The new hardware redesign and the new steps in the measurement and the calibration processes have been detailed. The system also incorporates analysis algorithms to evaluate the reliability of the reported values. All these changes result in a precision of 0.5% in the weighted solar attenuation value and the capability to report confidence intervals for each value in real time, which is a useful tool for the operation of CSP.

Spectral atmospheric extinction measurement in the solar wavelength range with a resolution of 0.25 nm in the VIS region is also achieved. This provides the capability to assess the different sources of attenuation, such as peaks of absorbance (Na, H, H_2O) or scattering, confirming the reliability of the method. Relevant spectral features in some specific weather conditions of humidity and haze have been reported as examples of the capacities of the system. This opens the way to experimentally obtain or validate the parameters used by the current atmospheric extinction simulation models. A 6-month long campaign of solar weighted atmospheric extinction measurements at an operating solar plant has also been reported.

Funding

This research did not receive any specific grant from funding agencies in the public, commercial, or not-for-profit sectors.

Data availability statement

The data presented in this study are available on request from the corresponding author. The data are not publicly available because it also forms part of an ongoing study.

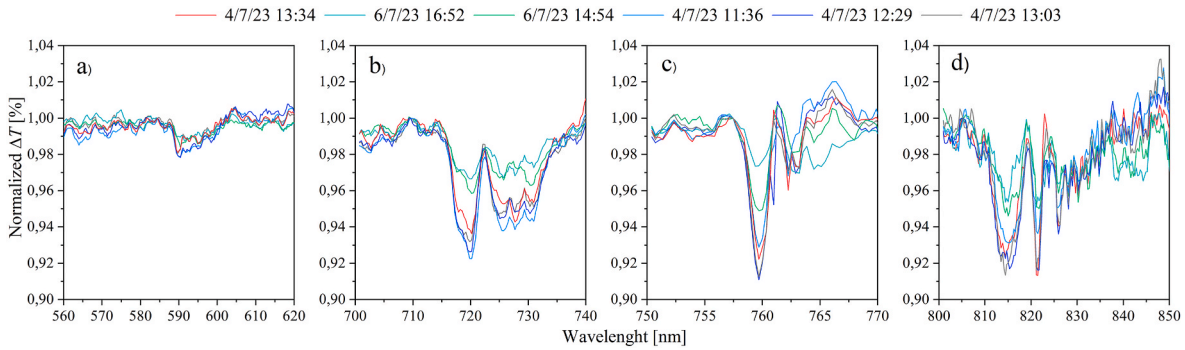

Fig. 13. Detail of absorption peaks a) Na 589 nm. b) H_2O 720 nm. c) O_2 759 nm. d) O_2 822 nm.

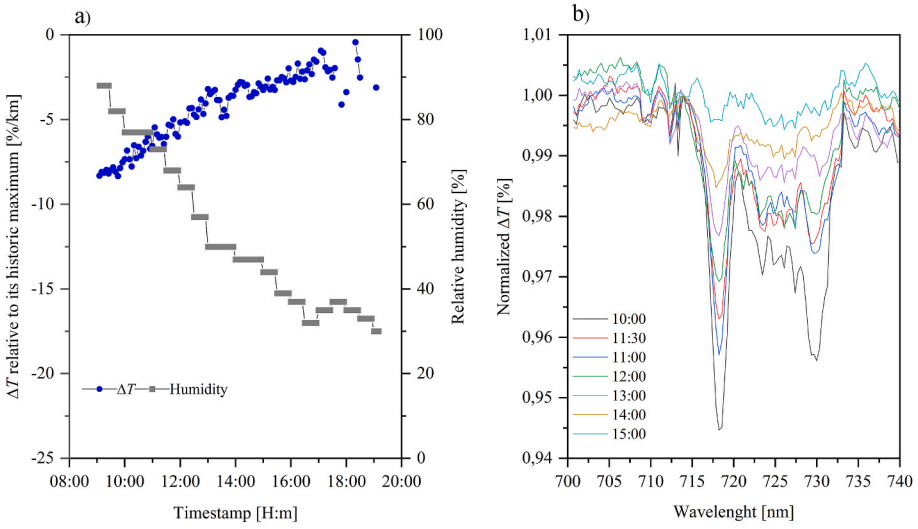

Fig. 14. a) Measured solar weighted atmospheric transmittance in day 1 (high humidity day) and relative humidity. b) Detail of the absorption peak of the H_2O at different hours.

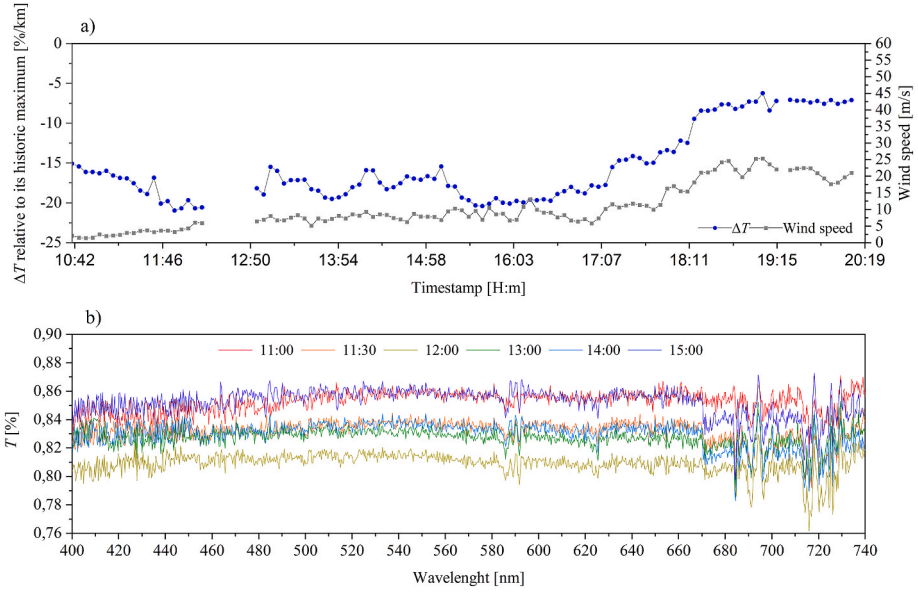

Fig. 15. a) Measured solar weighted atmospheric transmittance in day 2 (haze day) and wind velocity. b) Detail of the measured spectra in the visible range at different hours.

CRediT authorship contribution statement

Carlos Heras: Investigation, Methodology, Resources, Supervision, Writing – original draft, Writing – review & editing. **Iñigo Salinas:** Software, Visualization, Writing – original draft, Writing – review & editing. **Salvador Andres:** Data curation, Formal analysis, Writing – original draft, Writing – review & editing. **Marina Sevilla:** Formal analysis, Visualization. **Asier Villafranca:** Project administration, Validation, Methodology. **David Martinez:** Data curation, Software, Visualization. **Marcelino Sanchez:** Conceptualization, Project administration.

Declaration of competing interest

The authors declare that they have no known competing financial interests or personal relationships that could have appeared to influence the work reported in this paper.

Acknowledgment

The authors would like to thank Atlantica Sustainable Infrastructure and Rioglass Services S.A. for making this work possible and the staff at PS10 for their assistance with the installation and maintenance of the system.

References

[1] A. Salmon, A. Marzo, J. Polo, J. Ballestrín, E. Carra, J. Alonso-Montesinos, World map of low-layer atmospheric extinction values for solar power tower plants projects, Renew. Energy 201 (2022) 876–888, https://doi.org/10.1016/j.renene.2022.11.003.

[2] J. Polo, J. Ballestrín, E. Carra, Sensitivity study for modelling atmospheric attenuation of solar radiation with radiative transfer models and the impact in solar tower plant production, Sol. Energy 134 (2016) 219–227, https://doi.org/10.1016/j.solener.2016.04.050.

[3] N. Hanrieder, S. Wilbert, D. Mancera-Guevara, R. Buck, S. Giuliano, R. Pitz-Paal, Atmospheric extinction in solar tower plants – a review, Sol. Energy (2017), https://doi.org/10.1016/j.solener.2017.01.013.

[4] B.R. Mishra, N. Hanrieder, A. Modi, S.B. Kedare, Comparison of three models to estimate the slant path atmospheric attenuation in central receiver solar thermal plants under Indian climatic conditions, Sol. Energy 211 (2020) 1042–1052, https://doi.org/10.1016/j.solener.2020.10.049.

[5] U. Ali Rahoma, A.H. Hassan, Determination of atmospheric turbidity and its correlation with climatologically parameters, Am. J. Environ. Sci. 8 (2012) 597–604, https://doi.org/10.3844/ajessp.2012.597.604.

[6] N. Hanrieder, M. Sengupta, Y. Xie, S. Wilbert, R. Pitz-Paal, Modeling beam attenuation in solar tower plants using common DNI measurements, Sol. Energy 129 (2016) 244–255, https://doi.org/10.1016/j.solener.2016.01.051.

[7] G.E. Shaw, J.A. Reagan, B.M. Herman, Investigations of atmospheric extinction using direct solar radiation measurements made with a multiple wavelength radiometer, J. Appl. Meteorol. (1973), https://doi.org/10.1175/1520-0450(1973)012<0374:ioaeud>2.0.co;2.

[8] C.C. Wen, H.H. Yeh, Comparative influences of airborne pollutants and meteorological parameters on atmospheric visibility and turbidity, Atmos. Res. 96 (2010) 496–509, https://doi.org/10.1016/j.atmosres.2009.12.005.

[9] Z.M. Tahboub, A.A. Al Obaidli, F. Luque, I. Salbidegoitia, O. Farges, Z. Hassar, A. Oumbe, N. Geuder, O. Goebel, Solar beam attenuation experiments – Abu Dhabi, in: SolarPACES Conference, 2012.

[10] J. Ballestrín, E. Carra, R. Monterreal, R. Enrique, J. Polo, J. Fernández-Reche, J. Barbero, A. Marzo, J. Alonso-Montesinos, G. López, F.J. Batlles, One year of solar extinction measurements at Plataforma Solar de Almería. Application to solar tower plants, Renew. Energy 136 (2019) 1002–1011, https://doi.org/10.1016/j.renene.2019.01.064.

[11] J. Ballestrín, R. Monterreal, M.E. Carra, J. Fernández-Reche, J. Polo, R. Enrique, J. Rodríguez, M. Casanova, F.J. Barbero, J. Alonso-Montesinos, G. López, J. L. Bosch, F.J. Batlles, A. Marzo, Solar extinction measurement system based on digital cameras. Application to solar tower plants, Renew. Energy 125 (2018) 648–654, https://doi.org/10.1016/j.renene.2018.03.004.

[12] C. Heras, I. Salinas, M. Sevilla, R. Chueca, S. Escorza, C. Fernández–Peruchena, A. Bernardos, P. Sevillano, M. Sánchez, Atmospheric attenuation measurement system for commercial solar plants based on optical spectrum analysis, Sol. Energy 236 (2022) 782–789, https://doi.org/10.1016/j.solener.2022.03.057. ISSN 0038-092X.

[13] P. Ineichen, Conversion function between the Linke turbidity and the atmospheric water vapor and aerosol content, Sol. Energy 82 (2008) 1095–1097, https://doi.org/10.1016/j.solener.2008.04.010.

[14] B. Molineaux, P. Ineichen, On the broad band transmittance of direct irradiance in a cloudless sky and its application to the parameterization of atmospheric turbidity, Sol. Energy 56 (1996) 553–563, https://doi.org/10.1016/0038-092X(96)00016-3.

[15] Z.M. Tahboub, A. Oumbe, Z. Hassar, A. Obaidli, Modeling of irradiance attenuation from a heliostat to the receiver of a solar central tower, in: SolarPACES Conference, 2013.

[16] S. Andres, C. Heras, J. García-Barberena, A. Bernardos, M. Sánchez, Spectrally-resolved Solar Radiation Attenuation Long-Term Monitoring Results in a Commercial Central-Receiver CSP Plant, SPIE Optical Engineering + Applications, 2023, pp. 12671–12677.

[17] C. Jacovides, D. Kaskaoutis, F. Tymvios, D. Asimakopoulos, Application of SPCTRAL2 parametric model in estimating spectral solar irradiances over polluted Athens atmosphere, Renew. Energy 29 (2004) 1109–1119. https://doi:10.1016/j.renene.2003.12.001.

[18] A. Berk, F. Hawes, Validation of MODTRANs6 and its line-by-line algorithm, J. Quant. Spectrosc. Radiat. Transfer 203 (2017) 542–556, https://doi.org/10.1016/j.jqsrt.2017.03.004.

[19] R.W. Bergstrom, P. Pilewskie, P. Russell, J. Redemann, T. Bond, P. Quinn, B. Sierau, Spectral absorption properties of atmospheric aerosols, Atmos. Chem. Phys. 7 (2007) 5937–5943, https://doi.org/10.5194/acp-7-5937-2007.

[20] A. Marzo, A. Salmon, J. Polo, J. Ballestrín, G. Soto, G. Quiñones, J. Alonso-Montesinos, E. Carra, M. Ibarra, J. Cardemil, E. Fuentealba, R. Escobar, Solar extinction map in Chile for applications in solar power tower plants, comparison with other places from sunbelt and impact on LCOE, Renew. Energy 170 (2021) 197–211, https://doi.org/10.1016/j.renene.2021.01.126.

[21] D. Kaskaoutisa, H. Kambezidisa, The role of aerosol models of the SMARTS code in predicting the spectral direct-beam irradiance in an urban area, Renew. Energy 33 (2008) 1532–1543. https://doi:10.1016/j.renene.2007.09.006.

[22] M. Collaud, E. Weingartner, D. Schaub, C. Hueglin, C. Corrigan, S. Henning, M. Schwikowski, U. Baltensperger, Saharan dust events at the Jungfraujoch: detection by wavelength dependence of the single scattering albedo and first climatology analysis, Atmospheric Chemistry and Physics, European Geosciences Union 4 (11/12) (2004) 2465–2480, https://doi.org/10.5194/acp-4-2465-2004,2004, 2004.

[23] R.W. Bergstrom, P. Russell, P. Hignett, Wavelength dependence of the absorption of black carbon particles: predictions and results from the TARFOX experiment and implications for the aerosol single scattering albedo, J. Atmos. Sci. 59 (3) (2002) 567–577, https://doi.org/10.1175/1520-0469(2002)059<0567:WDOTAO>2.0.CO.